Displaying quasi-brittle failure using avalanches: paper as a material model

François Villette, Julien Baroth, Frédéric Dufour, Sabine Rolland du Roscoat

Displaying quasi-brittle failure using avalanches: paper as a material model

François VILLETTE [a], Julien BAROTH [a], Frédéric DUFOUR [a], Sabine ROLLAND DU ROSCOAT [a]

[a] Univ. Grenoble Alpes, CNRS, Grenoble INP[1], 3SR, F-38000 Grenoble, France, UMR 5521

Corresponding author: Julien Baroth (email: julien.baroth@univ-grenoble-alpes.fr)

Abstract:

This article aims to discuss and complete the avalanche representations of the failure process of quasi-brittle materials. Paper was used as a model material. We proposed an original method to determine avalanches extracted directly from the force drops in the post-peak regime of experimental force-displacement curves. We studied the avalanche distributions on notched and unnotched samples, taking into account the measurement noise. From these experimental tests, two regimes in the avalanche distribution were observed during the propagation of a macrocrack, in particular with a well-defined power law at small scale, that was consistent with other avalanche distributions based on other methods and other materials in literature. A single regime power-law distributed was found for a diffuse damage (without a significant macrocrack propagation) using the Mazars' damage model. Our results showed that the post-peak regime of tensile curves contained the statistical signature of the propagation of a macrocrack during the rupture of paper.

Keywords: Crack propagation, quasi-brittle materials, avalanche distribution, paper material

Statements and declarations

- **Competing Interest:** the authors declare no competing financial or non-financial interest.

Acknowledgements

Laboratoire 3SR is part of the LabEx Tec 21 (Investissements d'Avenir - Grant agreement n° ANR-11-LABX-0030) and of the PolyNat Carnot Institute (Investissements d'Avenir - Grant agreement no. ANR-16-CARN-0025-01). The authors gratefully acknowledge the LGP2 (Laboratoire de Génie des Procédés pour la Bioraffinerie, les Matériaux Bio-sourcés et l'Impression Fonctionnelle) for allowing us to use their test equipment.

[1] Institute of Engineering Univ. Grenoble Alpes

1. Introduction

This article raises the issue of the propagation of cracks in quasi-brittle materials. It is commonly explained that the microscopic behavior, $i.e.$ the successive apparitions, nucleations, bifurcations and stops of microcracks is at the origin of the progressive development of the Fracture Process Zone (FPZ) just before the localization in macroscopic cracks (Bažant 1994). This discrete propagation in time (the so-called avalanches) of the microcracks under a quasi-static loading is due to the discrete distribution in space of the material properties (heterogeneities). This is the main reason why in all quasi-brittle materials, the size of the FPZ is strongly related to the microstructural sizes even though the shape of the stress field may also affect the FPZ width (Giry et al. 2011).

The size of the FPZ is a key parameter for the objective modelling of structural failure. In a quasi-static loading, all regularization techniques and more generally objective constitutive models must include at least one internal length to represent the dissipative process taking place in the FPZ and thus avoiding any mesh dependency. However, in the best knowledge of the authors, no explicit relation between the internal length of a model and some characteristic sizes of the material does exist. It can be done by inverse analysis on structural failure at different scales (Le Bellégo et al. 2003). Identifying in a simple manner, precise though, the model internal length as a function of geometrical quantities to be set in the numerical model remains a scientific challenge.

In order to better understand and describe this propagation, the acoustic emission (AE) technique allows representing a series of microscopic ruptures (Saha and Vidya Sagar 2022). However, such studies involve complex, time-consuming technologies and processes. First, the spatial distribution of acoustic events in 2D or even 3D must be projected along a profile perpendicular to the macrocrack. Histograms based on either the number and/or the energy of acoustic events are drawn. Then, distribution laws must be fitted on this histogram to get a characteristic width of the FPZ.

Using a procedure originally developed to locate earthquakes, AE arrival-time data can be inverted to obtained spatial locations of microevents (Lockner et al. 1991). AE allows recording the properties and the localization of fracture precursors on heterogeneous materials. It is often found that the microcracks cluster together as the load increases and the instantaneous acoustic energy follows a power law distribution. The statistical analysis of the failure process of different materials shows that the distribution of rupture events may be displayed using power laws (Gutenberg and Richter 1944) (Voight 1988). Power laws were observed using AE on various materials as rocks (Grasso and Sornette 1998) (Diodati et al. 1991), polymers (Petri et al. 1994) (Deschanel et al. 2009), sandstone (Fortin et al. 2009), concrete (Alam et al. 2014), wood (Guarino et al. 2002) or paper (Salminen et al. 2002). The power law distribution of earthquake sizes is well known (Gutenberg and Richter 1944). For dozens years, the power law distributions of avalanche sizes and energies were observed and modelled (Girard et al. 2010). The Gutenberg-Richter law points out that the energy generated by rupture events

follows the relation $p(E) \sim E^{-\beta}$, with β values between 1.2 and 2 have been reported for various materials (Diodati et al. 1991; Garcimartín et al. 1997). It has also been observed that the time lag τ between two rupture events follows a power law (Voight 1988) $p(\tau) \sim \tau^{-\alpha}$, with α values can be found between 1 and 1.5.

Power laws may also be seen when analysing the force of velocity fluctuation in a failure test. Among many other, Santucci et al. exhibited power-laws in avalanche distributions from velocity of crack front during its propagation in heterogeneous interface (Santucci et al. 2018). Barés et al. showed that for a fracture test of an artificial rock, the power release determined from the response curve is a power law distributed in two regimes (Barés et al. 2014).

Avalanche distributions were extensively theoretically studied using Fiber Bundle Models (Daniels 1945; Hemmer and Hansen 1992; Zapperi et al. 1999). In particular, the two power-law distribution observed by Barés et al. (2014) during crack propagation was observed using Fiber Bundle Models in the study of imminent failure of the bundle (Pradhan et al. 2005) and on breakdown phenomena with crack propagation for elastic (Delaplace et al. 2001), visco-elastic (Baxevanis et al. 2006) materials with random distributed properties as well as materials with structural heterogeneities (Villette et al. 2020).

This article deals with the description of rupture events in tensile failure of paper samples. Paper was used as a model material. Avalanches were extracted directly from force drops in experimental force-displacement curves. In the following section, the proposed method to study avalanche distributions is presented. This approach was applied to tensile tests on notched and unnotched paper samples. Then, results are studied and discussed.

2. A new and simple experimental approach to study avalanche distributions

In this section, we propose to highlight power law distributions observed without AE during the post-peak regime of paper samples in a tensile failure test. The aim is to study the statistics of the force drops in the post-peak regime on the global response of a structure on a failure test. The experimental setup is first described. Avalanches are then defined using force drops extracted from the force-displacement curve.

2.1. Experimental setup

The reference paper used for this study was made of softwood fibers and manufactured with a Rapid-Köthen sheet former. According to standards, the paper thickness (ISO 534:2011(F)) was equal to 127 μm and its basis weight (ISO 536:2019) was equal to 60 $g.m^{-2}$.

In order to study the influence of crack propagation on the statistics of the force drops, mechanical tests were carried out on notched (more likely to propagate a single crack) and unnotched (more likely to develop diffuse damage) rectangular samples (20 mm in height and 35 mm in width) cut with a razor blade within the paper sheet. The chosen dimensions of the samples ensured a quasi-static failure with a displacement driven test. Indeed, for larger specimens, due to size effects, some unstable failures were obtained. The notch was cut at the middle right of the sample and was 15 mm long, that was sufficiently long to initiate failure at the notch tip. For a shorter notch, the paper heterogeneities may have triggered the failure away from the notch.

Fig. 1 shows a schematic view of the mechanical setup. Displacement controlled tensile tests were conducted on the Instron® 3365 machine at a speed of 4 $mm.min^{-1}$, equipped with a 10 kN force sensor at 100 Hz of acquisition rate. The samples were stored before the mechanical testing in a controlled environment of 23°C and 50% of relative humidity and released just prior the tensile test.

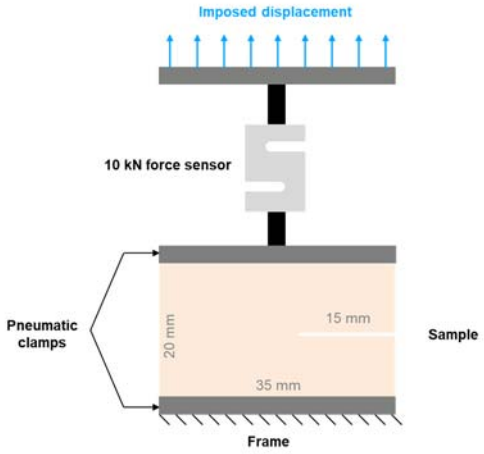

Fig. 1 Setup of the tensile test on a paper sample.

2.2. Avalanches in the post-peak

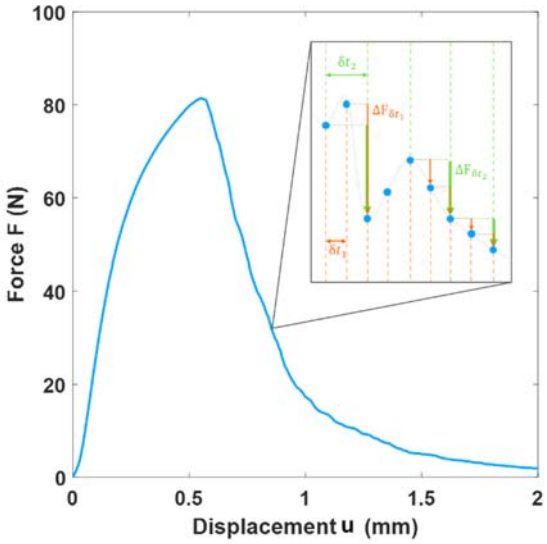

Fig. 2 Typical force-displacement ($\boldsymbol{F}$,$\boldsymbol{u}$) tensile curve of a $\boldsymbol{60\ g.m^{-2}}$ paper. The insert is a zoom on the curve in the post peak regime. Each point of the curve (blue points) corresponds to an acquisition by the sensors in displacement and force. The arrows represent avalanches $\boldsymbol{\Delta F_{\delta t_i}}$ over the time increment $\boldsymbol{\delta t_i}$. The resulting avalanches are shown for two different time increments: (in orange) $\boldsymbol{\delta t_1}$, corresponding to the acquisition rate, and (in green) $\boldsymbol{\delta t_2 = 2 \times \delta t_1}$.

Fig. 2 shows a typical force-displacement curve obtained on the tested paper samples. Let us call $\{u_t, F_t\}$ the sequences of measurement points acquired by both sensors in displacement and in force during the test, respectively, where t was the time at measurement. Giving a time increment δt, taken as a multiple of the acquisition rate during the test, we defined avalanches as force drops such as: an avalanche occurred at the point $\{u_t, F_t\}$ when $F_{t+\delta t} - F_t < 0$. The corresponding size of the avalanche was the force drop $\Delta F = F_t - F_{t+\delta t}$. The insert of the Fig. 2 shows some examples of considered avalanches, denoted $\Delta F_{\delta t_1}$ and $\Delta F_{\delta t_2}$, for two time increments δt_1 and δt_2, respectively. Taking into account all avalanches occurring after the peak, the distribution of the number $N_{\Delta F}$ of observed avalanches of size ΔF was derived.

2.3. Characterization of the avalanche distribution caused by measurement noise

Some similar works, *e.g.* (Barés et al. 2014), pointed that the smallest avalanches in the obtained distribution highlighted a Gaussian shape. They assumed that it was due to the measurement noise. Therefore, it seemed necessary to account for it before going further in the study of the avalanche distribution. In order to quantify the influence of the measurement noise in the force signal, we recorded the force cell signal during an empty tensile test, *i.e.*, without specimen between clamps, at the same speed and during a time period in the same order of rupture tests carried out.

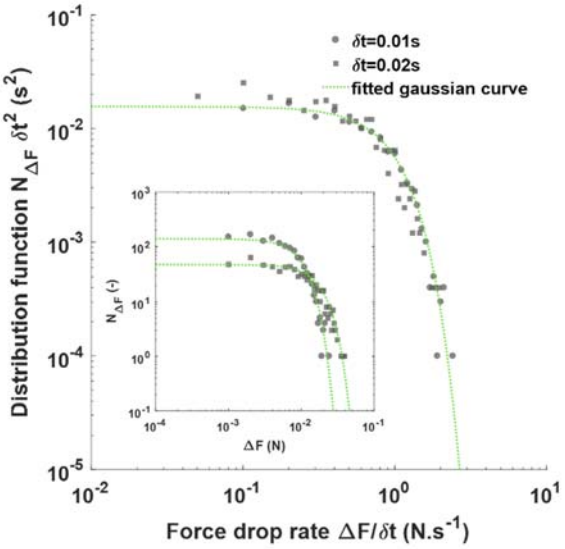

Fig. 3 Distributions of the number $\boldsymbol{N_{\Delta F}}$ of avalanches according to their size $\boldsymbol{\Delta F}$ derived from the signal recorded by the force sensor during an empty test, for two time increments $\boldsymbol{\delta t}$ ($\mathbf{0.01}\ \boldsymbol{s}$ and $\mathbf{0.02}\ \boldsymbol{s}$). The distributions are normalized by $\boldsymbol{\delta t}$ which makes them collapse on a unique master curve. The green dotted curve is a Gaussian curve of zero mean and a standard deviation fitted on the results. The insert shows the distribution without normalization.

Fig. 3 shows the distribution of avalanches from the empty test according to the method presented in the previous section. The distributions were displayed for two time increments δt ($0.01\ s$ and $0.02\ s$) and normalized by δt. Due to the signal noise, they exhibited a centered Gaussian shape with a standard deviation σ_G of $0.7\ N.s^{-1}$ approximatively.

3. Results of tensile tests on paper samples and discussion

Tensile tests were conducted on notched and unnotched paper samples (six of each). First, the global avalanche distributions for the notched and unnotched samples are shown before discussing the influence of the crack propagation on the avalanche distributions. The shape of the avalanche distributions is then after discussed in comparison with the one obtained from a continuous damage model with a softening behavior.

3.1. Global avalanche distributions

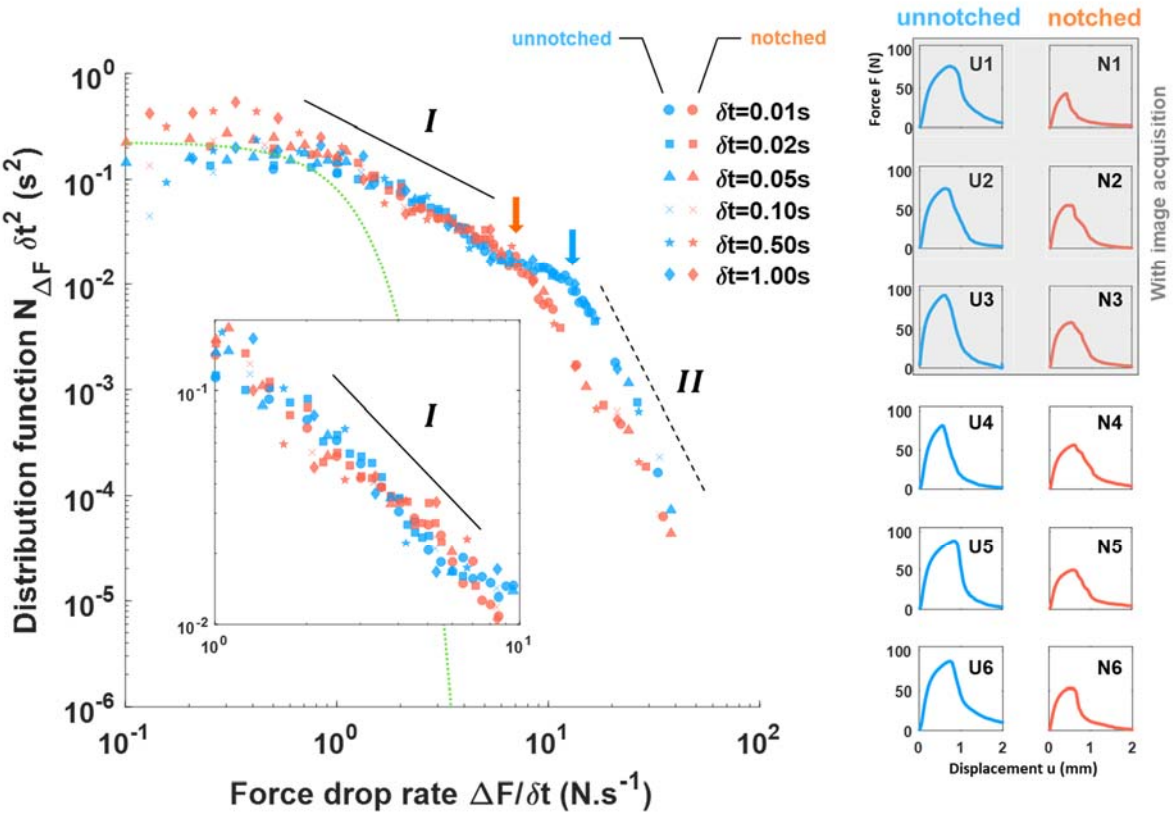

Fig. 4 Distribution of the number $N_{\Delta F}$ of avalanches according to their size ΔF for unnotched (blue points) and notched (orange points) samples for several time increments δt. The distributions are normalized by δt. The distributions exhibit two different regimes highlighted at small I and large scales II. The force drop rate at crossover of the two regimes is marked by the vertical arrows. The green dotted curve is the fitted Gaussian curve obtained from the empty test. The curve is shifted vertically to match smaller scales of distributions for the sake of clarity. The insert shows zoom on the first regime. The tensile curves of all samples are shown in the right columns.

Fig. 4 shows the avalanche distributions for the notched and unnotched paper samples, each distribution was the sum of the one over six samples. Each distribution was displayed for several time increments δt. The distributions collapsed into a single master curve when normalized by δt. A plateau was observed at the smaller scales of the distributions, which corresponded to scales dominated by the sensor noise. The Gaussian distribution found for the empty test was displayed and vertically shifted to match with the smaller scales of the distributions for the sake of clarity. These scales were then not considered in the further analysis of the results.

On the relevant part, the distributions exhibited two regimes at small (I) and large (II) scales. The small-scale regime was power law distributed (see insert of Fig. 4). Using least square method, the scaling exponent found for both distributions at small scales were the same and equal to -1.1 ± 0.1 (scaling exponent 95% confidence interval). At large scale, we measured avalanches that seemed to follow a second regime (II). As large-scale avalanches were spread over a narrow interval, it was difficult to determine the shape of the second

regime with any certainty. It could be an exponential cut-off, as generally observed for avalanche distributions (Santucci et al. 2018) or a power law as supported by the available literature on avalanche distribution from crack propagation in fracture experiment carried out on artificial rocks (Barés et al. 2014) or using heuristic models of crack propagation based on Fiber Bundle Models with structural heterogeneities (Villette et al. 2020) or purely randomly distributed (Delaplace et al. 2001). Future investigations could enable us to determine the precise shape. Nevertheless, in order to give at least an order of magnitude on the differences with regime I, we assumed that large avalanches were power law distributed to determine an apparent scaling exponent.

The found apparent scaling exponent at large scale were -4.2 ± 0.3 and -3.6 ± 0.2 for the unnotched and notched samples, respectively. The cutting force drop rate $\Delta F_c/\delta t$, *i.e.,* at the crossover of the two regimes (vertical arrows in Fig. 4), was smaller for the notched samples than for the unnotched ones, equal to 8 and 13 $N.s^{-1}$, respectively.

The scaling exponents, the considered range of avalanche and the R-square value in each case are summarized in Tab. 1.

Here, we extended observation of the two regime profiles on avalanches simply based on the force drops in post peak of tensile curve of paper material.

	Small scales (I)			**Large scales (II)**		
	Scaling exponent	Range	R-square	Apparent scaling exponent	Range	R-square
Unnotched	-1.1 ± 0.1	$[\sigma_G, \Delta F_c/\delta t]$	0.96	-4.2 ± 0.3	$> \Delta F_c/\delta t$	0.93
Notched	-1.1 ± 0.1	$[\sigma_G, \Delta F_c/\delta t]$	0.98	-3.6 ± 0.2	$> \Delta F_c/\delta t$	0.98

Tab. 1 Scaling exponent $\pm$ **95%** confidence interval at small and large scales determined by the least square method with the considered range and the R-square for the avalanche distribution of the unnotched and notched samples.

3.2. Influence of the crack propagation of the stress drop distribution

Fig. 5 exhibits the avalanche distributions for three unnotched specimen (U1, U2 and U3) and three notched ones (N1, N2, N3). Four step images of the rupture tests are depicted on the right of each avalanche distribution. Point-to-point image differences are also depicted in order to qualitatively highlight crack propagation in a clear manner.

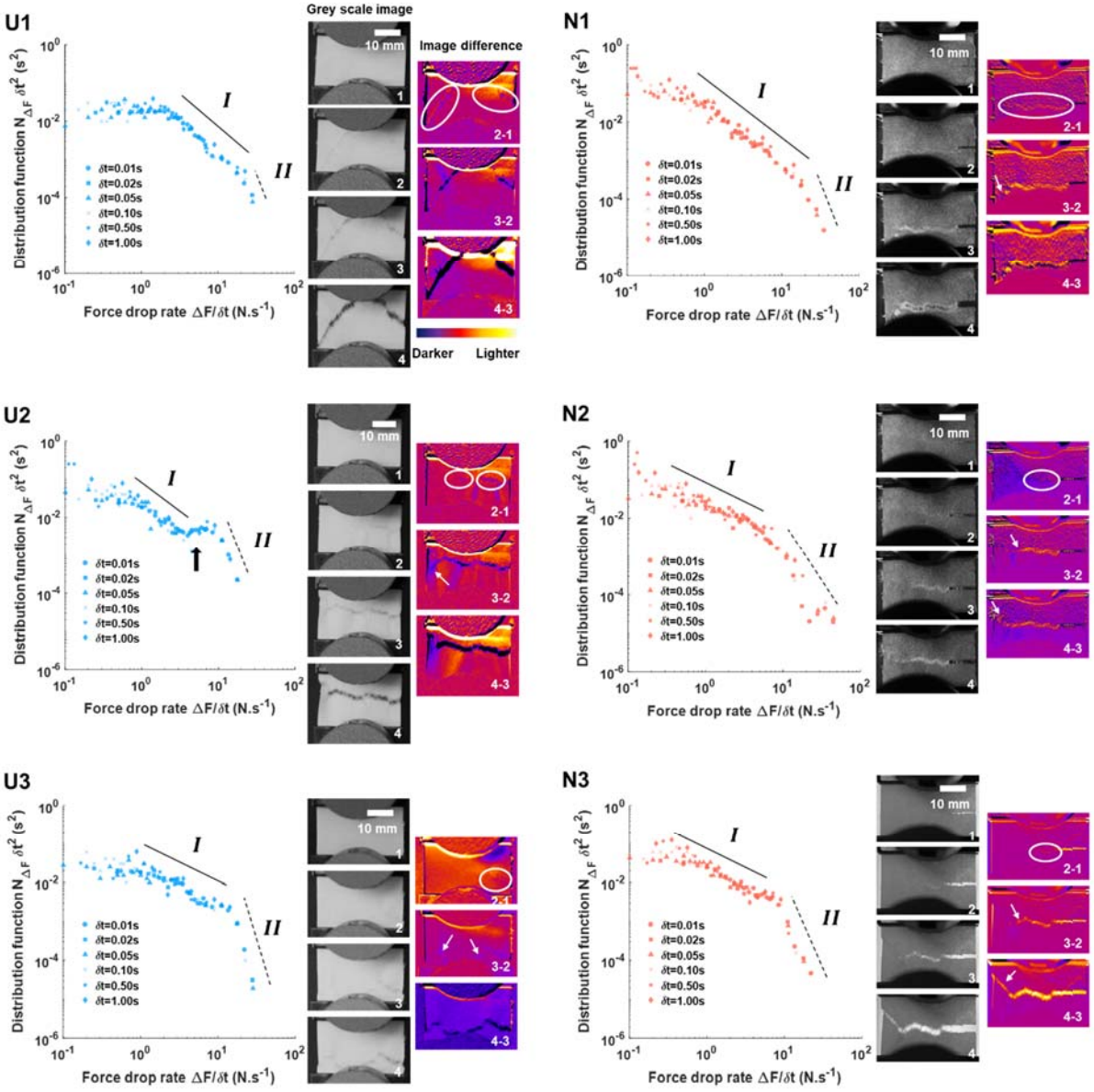

Fig. 5 Distribution of the number $N_{\Delta F}$ of avalanches according to their size ΔF for the unnotched samples U1, U2 and U3 (left) and notched samples N1, N2 and N3 (right), for different time windows δt. The distributions are normalized by δt. Grey scale images of each sample are shown at four steps of the rupture. The corresponding image differences are shown with arbitrary scale. Areas where damage occurs are pointed out by white arrows if small and surrounded by white circles if large.

For the samples U1 and N1, the avalanche distributions were dominated by the regime *I*, the regime *II* was relatively small or almost non-existent. At the onset of the fracture tests, cracks initiated on large zones all along the samples as roughly outlined by the white circles on image differences of U1 and N1. Accordingly, microcracks were spread throughout the sample width, then they coalesced without the propagation of a clear macrocrack. On the other samples (U2, U3, N2 and N3), the avalanche distributions exhibited more clearly two regimes. During fracture on these samples, the damage initiation was located on a single side (notch tip for notched ones) and progressively a macrocrack propagated through the sample width (white arrows on image

differences). On U2, we also observed a plateau between regimes *I* and *II* (arrow on avalanche distribution). This behavior was not observed on other samples and its causes were not well understood so far. Zoom on regime *I* of each avalanche distribution is shown in supplemental information (Fig. 8).

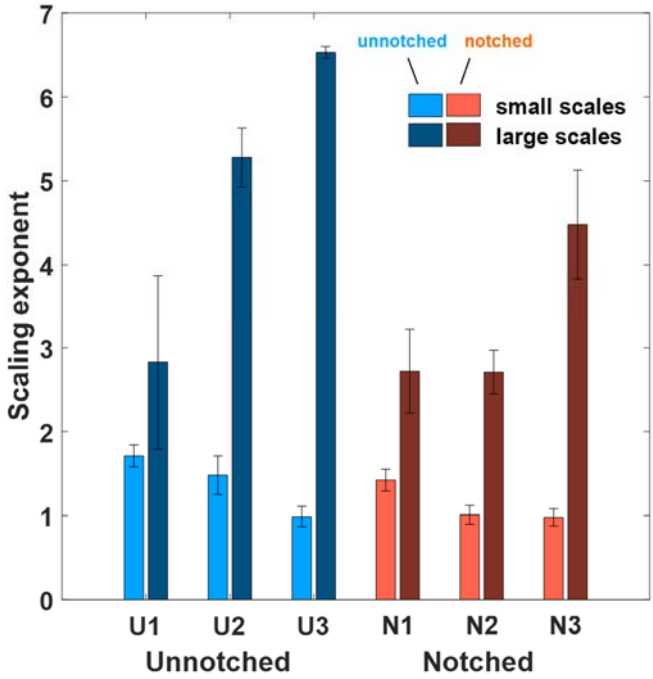

Fig. 6 Scaling exponent of the small and large scales for U1, U2, U3, N1 N2 and N3 samples. Error bars represents the **95**% confidence intervals.

Fig. 6 shows the scaling exponents at small and large scales for the unnotched and notched samples determined by the least-square method. For both types of samples, higher was the large-scale exponent, smaller was the small-scale exponent. It should be noted that the first regime (small avalanches) is the one of diffuse damage and the second regime (large avalanches) is the one of the propagation of a macrocrack with a stress concentration and therefore a less spatially spread FPZ. Thus, it seems reasonable that a competition between the two mechanisms may occur. Either we have a macrocrack initiated from the notch and then the microcracks are limited to the crack tip, or various small heterogeneities are at the onset of microcracks, that are gradually activated such that a coalescence can be finally observed.

The scaling exponents, the considered range of avalanche and the R-square value in each case are summarized in Supplemental Information (Tab. 3). The boundary between regimes *I* and *II* that was used to determine

scaling exponents was equal to the corresponding cutting force drop rates $\Delta F_c/\delta t$ found in the previous section, except for U2 because of the plateau in the avalanche distribution.

3.3. Discussion about the shape of the avalanche distributions by means of a continuous damage model

In this section, we studied the theoretical avalanche distributions of a quasi-brittle material using the Mazars' damage model.

In continuous damage model, the progressive degradation of the material may be represented by a damage scalar variable D in the constitutive law linking the Cauchy stress tensor $\boldsymbol{\sigma}$ and the small strain tensor $\boldsymbol{\varepsilon}$ by:

$$\sigma_{ij} = (1 - D)C_{ijkl}\varepsilon_{kl} \tag{1}$$

where σ_{ij} and ε_{kl} are the components of the stress and strain tensors, respectively. C_{ijkl} corresponds to the components of the stiffness tensor. The damage variable D varies during the loading from 0 (sound material) to 1 (fully damaged material).

Assuming uniaxial loading, the projection of the constitutive law (1) on the axial direction, *i.e.,* tensile direction, is:

$$\sigma = \frac{F}{wt_h} = (1 - D)E\varepsilon = (1 - D)E\frac{u}{l_0} \tag{2}$$

where $\sigma = \frac{F}{wt_h}$ and $\varepsilon = \frac{u}{l_0}$ are the macro stress and the macro strain and E the Young's modulus of the material. w, t_h, l_0 are the sample initial width, thickness and height, respectively.

In the Mazars' damage model, the evolution of the damage variable D in uniaxial traction depends on the axial strain ε:

$$\begin{cases} D(\varepsilon < \varepsilon_{d0}) = 0 \\ D(\varepsilon \geq \varepsilon_{d0}) = 1 - \dfrac{\varepsilon_{d0}(1 - A_t)}{\varepsilon} - \dfrac{A_t}{e^{B_t(\varepsilon - \varepsilon_{d0})}} \end{cases} \tag{3}$$

involving three parameters ε_{d0}, A_t, B_t. The parameter ε_{d0} corresponds to the strain at the damage initiation. The parameter A_t controls the residual stress when damage tends towards unity and B_t manages the post-peak shape (*i.e.,* brittleness) of the tensile curve.

Assuming zero residual stress (*i.e.*, $A_t = 1$) and combining (2) and (3), the equation of the theoretical force displacement curve obtained with the Mazars' damage model for a tensile test is:

$$\begin{cases} F(u < u_{d0}) = Cu \\ F(u \geq u_{d0}) = e^{-B_t(\varepsilon - \varepsilon_{d0})} \times \dfrac{Ewt_h}{l_0} u = e^{-B_{t0}(u - u_{d0})} \times Cu \end{cases} \quad (4)$$

with $B_{t0} = \frac{B_t}{l_0}$, $u_{d0} = \varepsilon_{d0} \times l_0$ and $C = \frac{Ewt_h}{l_0}$.

The obtained curves following (4) have a softening strictly monotonic decreasing post-peak, devoid of fluctuation as the Mazars' model does not take heterogeneities into account. Nevertheless, for a given discretized curve, the post-peak shows force drops by definition. Therefore, the force drops can be studied in the same methodology than described in section 2.2 to derive the avalanche distribution.

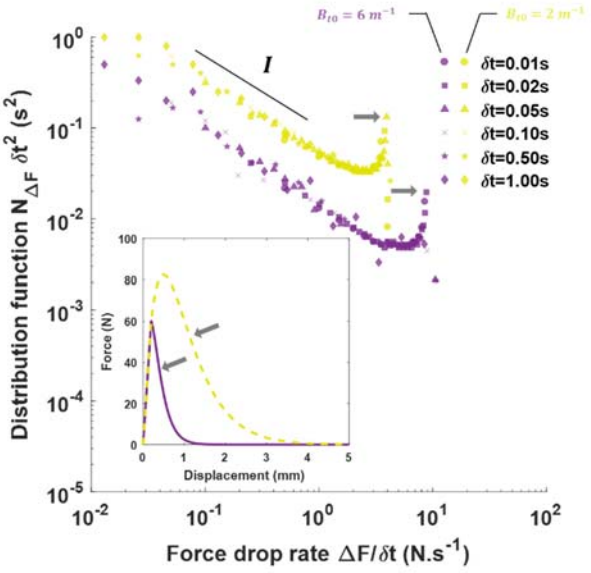

Fig. 7 Distribution of the number $\boldsymbol{N_{\Delta F}}$ of avalanches according to their size $\boldsymbol{\Delta F}$ for the Mazars' damage model with $\boldsymbol{B_{t0} = 6\ m^{-1}}$ (purple points) and $\boldsymbol{2\ m^{-1}}$ (yellow points) for several time increments $\boldsymbol{\delta t}$. The distributions are normalized by $\boldsymbol{\delta t}$. The distributions exhibit a slope highlighted at small scale $\boldsymbol{I}$. The corresponding tensile curve of the Mazars' damage model is shown in the insert (solid curve for $\boldsymbol{B_{t0} = 6\ m^{-1}}$ and broken curve for $\boldsymbol{B_{t0} = 2\ m^{-1}}$).

Fig. 7 shows the avalanche distributions of two theoretical tensile curves (in the insert of Fig. 7) obtained using the Mazars' damage model (4). For the two curves, C was arbitrarily taken equal to $300\ N.mm^{-1}$. Giving that C is a constant prefactor in (4), its value did not influence neither the shape nor the scaling exponent of the avalanche distributions. The displacement at onset of damage u_{d0} was taken equal to $0.2\ mm$ which is on the order of magnitude of the displacement found at peak-load in experiments. Two values of B_{t0} ($2\ m^{-1}$

and 6 m^{-1}) were investigated in order to generate the tensile curves with more or less brittleness in the post-peak. The tensile curves had the same acquisition parameters than in the experiments, *i.e.,* 100 Hz.

	Scaling exponent	**Range**	**R-square**
Mazars' model ($B_{t0} = 6\ m^{-1}$)	-0.8 ± 0.1	$[0.1, 1]$	0.89
Mazars' model ($B_{t0} = 2\ m^{-1}$)	-0.8 ± 0.1	$[0.1, 1]$	0.98

Tab. 2 Scaling exponent $\pm$ **95%** confidence interval determined by the least square method with the considered range and the R-square for the avalanche distributions of the Mazars' damage model with $B_{t0} = 2\ m^{-1}$ and 6 m^{-1}.

Both avalanche distributions exhibited a similar shape with a single power law (I) excepted for the larger force drop rates, where number of avalanches increased due to inflection point in the post-peak (arrows on distributions and curves). The scaling exponent was determined by the least square method and equal to -0.8 in both cases. The scaling exponents, the considered range of avalanches and the R-square value in each case are summarized in Tab. 2.

The shape of the avalanche distributions may be summarized as follow:

- For a quasi-brittle material, due to the softening behavior, avalanches occurred during post peak with a power-law distribution of scaling exponent equal to -0.8. As material heterogeneities were not explicitly represented, the damage corresponded to the global degradation of the material *i.e.,* without damage localisation and crack propagation. This result was consistent with our experimental observations on the paper samples for which the onset of damage occurred on a large zone (*i.e.*, more diffuse) rather than at the tip of a macrocrack (*i.e.*, localised manner). In this particular experimental case, it is reminded that the avalanche distributions were dominated by a single power-law. Literature on Fiber Bundle Models also states the single power law of the avalanche distribution in the case of tensile test (Hemmer and Hansen 1992).
- On the tested samples, damage with a macrocrack propagation during fracture was correlated with two regimes, assumed two power laws, in the avalanche distribution. This observation was supported by theoretical studies on ZIP model (Delaplace et al. 2001; Villette et al. 2020) or in experiments on artificial rocks (Barés et al. 2014). Furthermore, we recently showed that the force drops that occurred during the post peak of a tensile curve can be related to the geometry of the active FPZ (Villette et al. 2023). Indeed, we characterised the FPZ geometry during fracture tests on paper samples and linked its size and form to the stress drops, considering the initial sample width and thickness for stress calculation, in the post peak regime. We showed that (i) the stress drops were proportional to the area of the FPZ activated during the considered drop and (ii) the active FPZ can take two possible forms, a circular one (at low stress drop) and a slenderer one in

the direction of the crack above a critical stress drop. Then, the FPZ geometry is related to the stress drops in the post-peak regime and the changing of the FPZ form could explain the bi-modal behavior in the avalanche distribution. It should be noted that the large scale exponents were widely dispersed and higher than those reported in the literature, which would be more in favor of an apparent exponent of a second exponential regime. Unless the definition of avalanches used here, which seems new in the literature, lead to higher coefficients than are known. In this publication, therefore, we assume an apparent coefficient, and remember that the important point is the presence of the large scale regime to a greater or lesser extent, correlated to crack propagation.

Therefore, we showed that tensile response curve contained the signature of the damage propagation studying the avalanche distribution that highlighted (i) a single regime for a diffuse damage or (ii) regimes for a macrocrack propagation.

4. Conclusion

This paper presented a statistical analysis of failure process in quasi-brittle materials using paper as a model material and based on the experimental study of the post-peak of the tensile response curve. Tensile tests on unnotched and notched paper samples were conducted. From the obtained tensile curves, we proposed a new approach of the avalanche statistics defined as the force drops of the global response in the post-peak regime. Considering all the samples, unnotched and notched separately, avalanche distributions exhibited two regimes: a well-defined power law at small scale and another regime at large scale, the shape of which remained difficult to access because of lake of data, but assumed in this publication power law distributed. In particular, the small scales exponent was equal to -1.1 and the cutting force drop was smaller for the notched samples than for the unnotched ones. The presence of the large-scale regime was correlated to the propagation of a macrocrack during failure of sample. Conversely, a diffuse damage over the sample width was associated with only a single regime power law distributed in the avalanche distribution. This observation was qualitatively consistent with the avalanche distribution predicted by the Mazars' damage model exhibiting a single power law for a diffuse damage. Therefore, our results showed that the post-peak of the tensile curve contained the statistical signature of a diffuse damage (single regime) and of macrocrack propagation (two regimes), the later was mainly activated during fracture tests on notched samples. Giving that force drops are related to the FPZ geometry, the form of the avalanche distribution could provide some useful information on the characteristic size involved during the material fracture and on the internal length used in nonlocal damage models. In future work, these results could be confirmed using more samples and could be extended on other quasi-brittle materials. A particular attention would be done to better characterize the large-scale regime. Numerical simulation using nonlocal damage models could be considered in order to study the influence of the internal length on avalanche distribution.

References

Alam SY, Saliba J, Loukili A (2014) Fracture examination in concrete through combined digital image correlation and acoustic emission techniques. Constr Build Mater 69:232–242. https://doi.org/10.1016/j.conbuildmat.2014.07.044

Barés J, Hattali ML, Dalmas D, Bonamy D (2014) Fluctuations of global energy release and crackling in nominally brittle heterogeneous fracture. Phys Rev Lett 113:1–5. https://doi.org/10.1103/PhysRevLett.113.264301

Baxevanis T, Dufour F, Pijaudier-Cabot G (2006) Interface crack propagation in porous and time-dependent materials analyzed with discrete models. Int J Fract 141:561–571. https://doi.org/10.1007/s10704-006-9013-x

Bažant ZP (1994) Nonlocal damage theory based on micromechanics of crack interactions. J Eng Mech 120:593–617

Daniels HE (1945) The statistical theory of the strength of bundles of threads. Proc, R Soc A183:405–435

Delaplace A, Roux S, Pijaudier-Cabot G (2001) Avalanche Statistics of Interface Crack Propagation in Fiber Bundle Model: Characterization of Cohesive Crack. J Eng Mech 9399:646–652. https://doi.org/10.1061/(ASCE)0733-9399(2001)127

Deschanel S, Vanel L, Godin N, et al (2009) Experimental study of crackling noise: Conditions on power law scaling correlated with fracture precursors. J Stat Mech Theory Exp 2009:P01018. https://doi.org/10.1088/1742-5468/2009/01/P01018

Diodati P, Marchesoni F, Piazza S (1991) Acoustic emission from volcanic rocks: An example of self-organized criticality. Phys Rev Lett 67:2239–2243. https://doi.org/10.1103/PhysRevLett.67.2239

Fortin J, Stanchits S, Dresen G, Gueguen Y (2009) Acoustic emissions monitoring during inelastic deformation of porous sandstone: Comparison of three modes of deformation. Pure Appl Geophys 166:823–841. https://doi.org/10.1007/s00024-009-0479-0

Garcimartín A, Guarino A, Bellon L, et al (1997) Statistical Properties of Fracture Precursors. Biophys Rev Lett 79:1–4

Girard L, Amitrano D, Weiss J (2010) Failure as a critical phenomenon in a progressive damage model. J Stat Mech Theory Exp 2010:P01013. https://doi.org/10.1088/1742-5468/2010/01/P01013

Giry C, Dufour F, Mazars J (2011) Stress-based nonlocal damage model. Int J Solids Struct 48:3431–3443. https://doi.org/10.1016/j.ijsolstr.2011.08.012

Grasso J-R, Sornette D (1998) Testing self-organized criticality by induced seismicity. J Geophys Res Solid Earth 103:29965–29987. https://doi.org/10.1029/97jb01344

Guarino A, Ciliberto S, Garcimartín A, et al (2002) Failure time and critical behaviour of fracture precursors in heterogeneous materials. Eur Phys J B 26:141–151. https://doi.org/10.1007/s10051-002-8953-9

Gutenberg B, Richter CF (1944) Frequency of earthquakes in California. Bull Seismol Soc Am 34:184–188. https://doi.org/10.1038/156371a0

Hemmer PC, Hansen A (1992) The Distribution of Simultaneous Fiber Failures in Fiber Bundles. J Appl Mech 59:909–914. https://doi.org/10.1115/1.2894060

Le Bellégo C, Dubé J, Pijaudier-cabot G, Gérard B (2003) Calibration of nonlocal damage model from size effect tests. Eur J Mech 22:33–46

Lockner D, Byerlee JD, Kuksenko V, et al (1991) Quasi-static fault growth and shear fracture energy in granite. Nature 350:39–42

Petri A, Paparo G, Vespignani A, et al (1994) Experimental evidence for critical dynamics in microfracturing processes. Phys Rev Lett 73:3423–3426. https://doi.org/10.1103/PhysRevLett.73.3423

Pradhan S, Hansen A, Hemmer PC (2005) Crossover behavior in burst avalanches: Signature of imminent failure. Phys Rev Lett 95:125501. https://doi.org/10.1103/PhysRevLett.95.125501

Saha I, Vidya Sagar R (2022) Statistical analysis of acoustic emission avalanches generated during the compressive fracture process, and Mode I fracture process in cementitious composites. Int J Fract 234:273–295. https://doi.org/10.1007/s10704-022-00618-2

Salminen LI, Tolvanen AI, Alava M (2002) Acoustic Emission from Paper Fracture. Phys Rev Lett 89:185503. https://doi.org/10.1103/PhysRevLett.89.185503

Santucci S, Tallakstad KT, Angheluta L, et al (2018) Avalanches and extreme value statistics in interfacial crackling dynamics. PhilTransR Soc A 377:20170394

Villette F, Baroth J, Dufour F, et al (2020) Influence of material heterogeneities on crack propagation statistics using a Fiber Bundle Model. Int J Fract 221:87–100. https://doi.org/10.1007/s10704-019-00409-2

Villette F, Dufour F, Baroth J, et al (2023) Interplay between structural scales and fracture process zone: experimental and numerical analysis on paper. Acta Mech. https://doi.org/10.1007/s00707-023-03576-5

Voight B (1988) A method for prediction of volcanic eruptions. Nature 332:125–130

Zapperi S, Ray P, Stanley HE, Vespignani A (1999) Avalanches in breakdown and fracture processes. Phys Rev E 59:5049–5057

Supplemental information

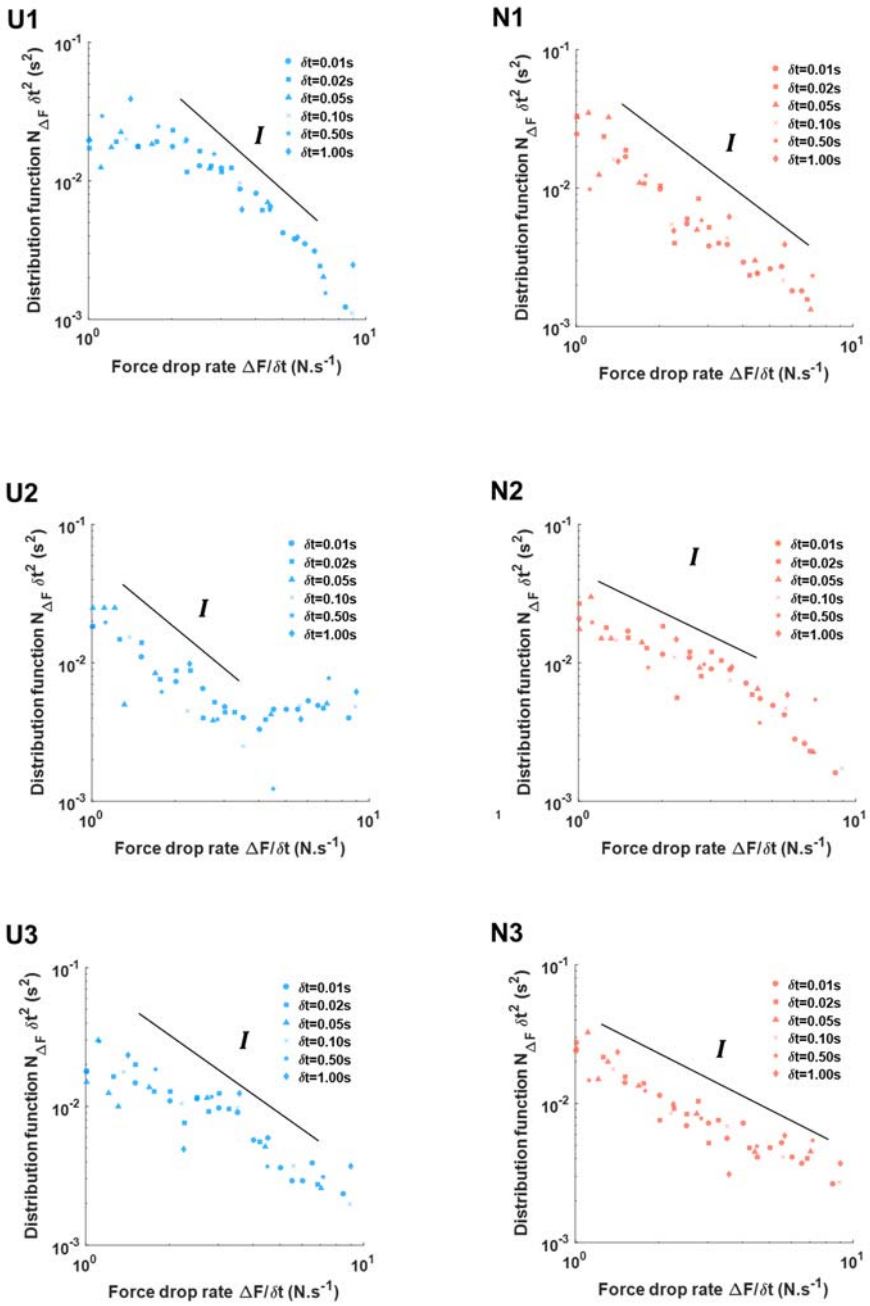

Fig. 8: Zoom on the small-scale regime (***I***) of avalanche distributions shown on **Fig. 5**.

	Small scales (I)			**Large scales (II)**		
	Scaling exponent	Range	R-square	Scaling exponent	Range	R-square
U1	-1.7 ± 0.1	$[1.5, \Delta F_c/\delta t]$	0.95	-2.8 ± 1	$> \Delta F_c/\delta t$	0.83
U2	-1.5 ± 0.2	$[\sigma_G, 3]$	0.84	-5.3 ± 0.4	> 10	0.99
U3	-1.0 ± 0.1	$[\sigma_G, \Delta F_c/\delta t]$	0.85	-6.5 ± 0.8	$> \Delta F_c/\delta t$	0.96
N1	-1.4 ± 0.1	$[\sigma_G, \Delta F_c/\delta t]$	0.91	-2.7 ± 0.5	$> \Delta F_c/\delta t$	0.90
N2	-1.0 ± 0.1	$[\sigma_G, \Delta F_c/\delta t]$	0.87	-2.7 ± 0.3	$> \Delta F_c/\delta t$	0.82
N3	-1.0 ± 0.1	$[\sigma_G, \Delta F_c/\delta t]$	0.88	-4.5 ± 0.7	$> \Delta F_c/\delta t$	0.96

Tab. 3 Scaling exponent $\pm$ **95**% confidence interval at small and large scales determined by the least square method with the considered range and the R-square for the avalanche distribution of U1, U2, U3, N1 N2 and N3 samples.